

# Numerical and Theoretical Considerations for the Design of the AVT-183 Diamond-Wing Experimental Investigations

Okko J. Boelens<sup>1</sup>

*National Aerospace Laboratory – NLR, Amsterdam, The Netherlands*

James M. Luckring<sup>2</sup>

*NASA Langley Research Center, Hampton, VA, 23681, USA*

Christian Breitsamter<sup>3</sup>, Andreas Hövelmann<sup>4</sup>, Florian Knoth<sup>5</sup>

*Technical University Munich, Munich, Germany*

Donald J. Malloy<sup>6</sup>

*Arnold Engineering Development Complex, Arnold Air Force Base, TN, 37389, USA*

Sébastien Deck<sup>7</sup>

*ONERA – The French Aerospace Lab, F-92190 Meudon, France*

**A diamond-wing configuration has been developed to isolate and study blunt-leading-edge vortex separation with both computations and experiments. The wing has been designed so that the results are relevant to a more complex Uninhabited Combat Air Vehicle concept known as SACCON. The numerical and theoretical development process for this diamond wing is presented, including a view toward planned wind tunnel experiments. This work was conducted under the NATO Science and Technology Organization, Applied Vehicle Technology panel. All information is in the public domain.**

## I. Nomenclature

$b/2$	wing semispan	$R_{c_{ref}}$	Reynolds number based on $c_{ref}$ , $U_{c_{ref}} / \nu$
$C_p$	static pressure coefficient	$R_{mac}$	Reynolds number based on $mac$ , $U_{mac} / \nu$
$C_{p,rms}$	rms fluctuating pressure coefficient	$r_{le}$	streamwise leading-edge radius
$c$	wing chord	$r_{ts}$	radius from test section centerline, Table 1
$c_r$	root chord	$St_c$	Strouhal number based on $c$ , $f c / U$
$c_{ref}$	reference chord	$s$	wing local semispan
$f$	frequency, Hertz	$t$	airfoil maximum thickness
$M$	Mach number	$U$	free stream reference velocity
$mac$	mean aerodynamic chord	$x,y,z$	body-axis Cartesian coordinates
$q_\infty$	free stream dynamic pressure, $\frac{1}{2} \rho_\infty U^2$		

<sup>1</sup> R&D Engineer, Applied Computational Fluid Dynamics, Department of Flight Physics and Loads, Aerospace Division, okko.boelens@nlr.nl.

<sup>2</sup> Senior Research Engineer, Configuration Aerodynamics Branch, james.m.luckring@nasa.gov, AIAA Associate Fellow.

<sup>3</sup> Chief Scientist, Institute of Aerodynamics and Fluid Mechanics, christian.breitsamter@aer.mw.tum.de, AIAA Associate Fellow.

<sup>4</sup> Research Engineer, Institute of Aerodynamics and Fluid Mechanics, andreas.hoevelmann@tum.de, AIAA Member.

<sup>5</sup> Research Engineer, Institute of Aerodynamics and Fluid Mechanics, florian.knoth@aer.mw.tum.de.

<sup>6</sup> Lead Aerodynamics Analysis Engineer, U.S. Air Force Analysis & Evaluation Branch, TSTA, donald.malloy.1@us.af.mil, AIAA Associate Fellow.

<sup>7</sup> Research Scientist, Applied Aerodynamics Department, sebastien.deck@onera.fr.

$\alpha$	angle of attack, deg.	$\mu$	viscosity
$\beta$	angle of sideslip, deg.	$\nu$	kinematic viscosity, $\mu/\rho$
$\eta$	fraction of wing semispan	$\rho$	density
$\Lambda$	wing sweep, deg.		

*Subscripts*

le	leading edge	te	trailing edge
max	maximum	$\infty, o$	free-stream reference conditions

*Acronyms*

AEDC	Arnold Engineering Development Complex, <i>USA</i>	RTO	Research and Technology Organization
AER	Institute of Aerodynamics and Fluid Mechanics	SA	Spalart-Allmaras turbulence model
AVT	Applied Vehicle Technology	SACCON	Stability And Control CONfiguration
DLR	German Aerospace Company, <i>Germany</i>	SST	Shear Stress Transport turbulence model
EADS	European Aeronautic Defence & Space Company	STO	Science and Technology Organization
NATO	North Atlantic Treaty Organization	TUM	Technical University Munich, <i>Germany</i>
NLR	National Aerospace Laboratory, <i>Netherlands</i>	UAV	Uninhabited Air Vehicle
ONERA	French Aerospace Laboratory, <i>France</i>	UCAV	Uninhabited Combat Air Vehicle
RANS	Reynolds Averaged Navier Stokes	ZDES	Zonal Detached Eddy Simulation

## II. Introduction

The advent of Uninhabited Air Vehicles (UAV, UCAV) has introduced performance opportunities along with some new aerodynamic challenges associated with the unique vehicle geometries for both conventional and in some cases expanded operating conditions. For example, laminar flow coupled with high-aspect-ratio wings can enhance loiter capability for some UAV concepts. In the case of UCAV concepts, the maneuver envelope can be expanded to higher-g conditions because the vehicle is uninhabited. Both classes of vehicles incorporate unique configuration features, and in the case of the UCAV, these include significantly altered planforms as compared to prior inhabited maneuvering aircraft as well as new design trades among aerodynamic, propulsion, and observable requirements.

The Stability And Control Configuration, SACCON, was developed to study dynamic stability characteristics of a representative UCAV concept with both experimental and computational activities. The SACCON configuration was also developed to be suitable for international collaboration such that significant resource sharing could be realized through a collaborative project coordinated through the Applied Vehicle Technology (AVT) Panel of the Research and Technology Organization (RTO), under the auspices of NATO. The project was known as AVT-161. An overview of this work has been published by Cummings and Schütte<sup>1</sup> [2012], and a full report<sup>2</sup> of the SACCON research project has been published through the RTO.

The SACCON wing aerodynamics encompass a suite of complex vortex flows and interactions. These include both sharp- and blunt-leading-edge vortices, vortex-vortex interactions, vortex breakdown, inner co-rotating vortices, and secondary vortices. All of these vortical flow physics are occurring on a twisted wing with only moderate sweep ( $\Lambda_{le} = 53^\circ$ ) and with a very nonlinear spanwise distribution of leading-edge radius. None of these complex vortical flows can be considered as having a validated CFD prediction capability, either as an isolated vortical phenomenon or as interacting vortical phenomena. Additional discussion of this complex flow has been given by Schütte<sup>3</sup> et al. [2012] among others.

The objective of the present work was to isolate as much as possible one particular vortex phenomenon, the onset and progression of blunt-leading-edge vortical separation, and to do so in a way that the flow physics would still be relevant to the SACCON wing flows. This would then enable an integrated numerical and experimental campaign to seek improved understanding and prediction capability of these flows.

The outcome of this effort was a particular diamond wing that could be considered either a combined-unit problem or perhaps a unit problem relevant to the more complex SACCON configuration as discussed by Luckring and Boelens<sup>4</sup> [2015]. Although the work was informed by CFD validation principles, it was not clear that all the current expectations for validation-class research could be met. However, it was felt that sufficient rigor could be brought to the problem at hand to obtain guidance for discriminating among various CFD methods as to why the methods should match or miss features of this flow that would come from new experiments. The work became part

of another collaborative research project identified as AVT-183 coordinated now through the STO. Reorganization in 2012 had established the STO as the successor organization from the RTO.

The remainder of this paper will address the process used for designing this research campaign. This includes Configuration Development [Section III], the Model Development [Section IV], and preliminary comments on the Experiment Development [Section V]. Details of the experiments will be addressed in two subsequent papers by Hövelmann<sup>5,6</sup> et al. [2015], and eight papers will follow summarizing the numerical findings<sup>7-14</sup> from the AVT-183 diamond wing investigations.

### III. Configuration Development

This particular diamond wing configuration was developed to be relevant to the more complex UCAV SACCON configuration. In this section the connection to this parent configuration is first reviewed. Next, the conceptual and CFD-based design approach that led to the AVT-183 diamond wing are presented. Finally the unsteady CFD analysis of the resultant wing is reviewed. The work was performed in preparation for the wind tunnel model development and testing. Additional details of this work have been given by Luckring and Boelens<sup>15</sup> [2011].

#### A. Connection to Parent AVT-161 SACCON Configuration

The SACCON configuration was designed by EADS and DLR to capture many aspects of UCAV aerodynamics while at the same time being suitable for international collaborative research. The configuration has an edge-aligned lambda-wing planform with a constant-chord outer panel, a leading-edge sweep of 53° and an aspect ratio of approximately 3.1, **Figure 1**. The configuration also incorporated a linear twist distribution outboard of the first trailing-edge break as well as fairly complex spanwise distributions of thickness and leading-edge radius, **Figure 2**. The thickness-to-chord ratio diminishes in the spanwise direction as does the leading-edge radius. In general, the leading-edge radii are less than 0.23% of the SACCON reference chord. The outboard twist delayed separation onset effects to higher angles of attack than would have been realized by a planar wing. Additional details can be found in Cummings and Schütte<sup>1</sup> [2012].



**Figure 1. SACCON configuration in the Low-Speed Wind Tunnel, Braunschweig Germany (DNW-NWB).  $\Lambda_{le} = 53^\circ$ .**

At low to moderate angles of attack the attached-flow design objective was achieved. However, subsequent vortical separation was very complex. A CFD example from Frink<sup>16</sup> [2010] is shown in **Figure 3**. Results were obtained with the RANS solver USM3D (Frink<sup>17</sup> [1992]) and the Spalart-Allmaras turbulence model. At the lower angle of attack shown, a sharp-leading-edge vortex is generated from the inboard portion of the leading edge, near the apex, while a blunt-leading-edge vortex is generated further outboard. Ahead of the blunt-leading-edge vortex is a region of attached flow near the leading edge, with some form of incipient separation flow physics near the origin of the blunt-leading-edge vortex. This region of attached flow and incipient separation, upstream of the outer vortex separation, is most curious, although the scale of the incipient separation flow physics is too small to see details in the figure. Additional analysis has indicated a possible third

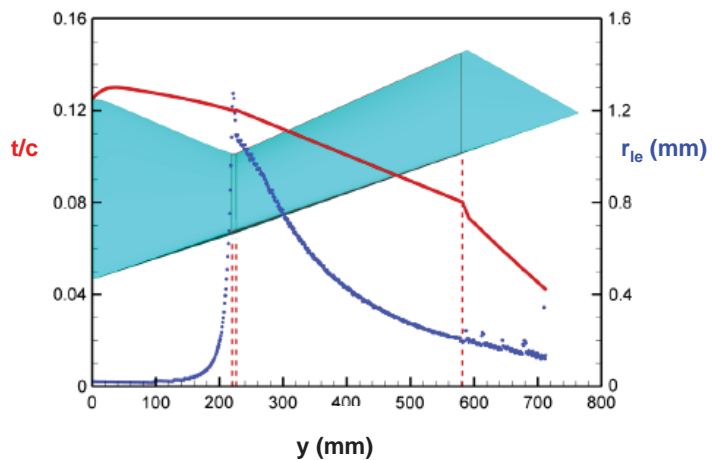
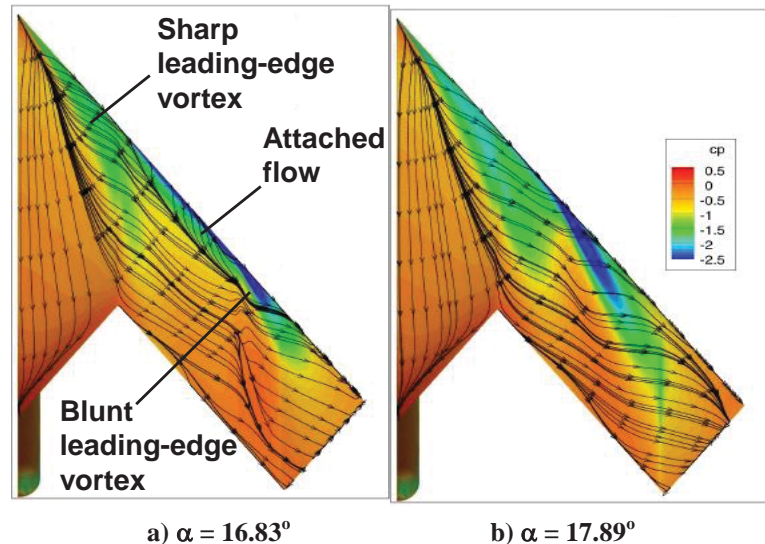


**Figure 2. Some geometric complexities of SACCON, from Cummings and Schütte<sup>1</sup> [2012].**

corotating vortex, slightly inboard of the outer vortex, which forms as part of the blunt-leading-edge separation. With an increase in angle of attack the origin of the blunt-leading-edge vortex separation moves upstream into the attached leading-edge flow, and by the angle of attack shown in Figure 3b no attached leading-edge flow region exists.

All of these vortex phenomena are interacting at the conditions shown; none of these phenomena, even in isolation, can be predicted with confidence using CFD. The conditions of Figure 3 also correspond to very nonlinear pitching moment effects, and thus are important to vehicle performance.

Given the complex nature of the vortical flows about the SACCON configuration, the current work was undertaken to isolate, as much as possible, one critical aspect of these flows in such a manner as to help discriminate why various CFD formulations differ as to their predictive capability. The phenomenon chosen was the onset and progression of blunt-leading-edge separation on the outboard portion of the wing. The location of the outer vortex is critical to any subsequent vortex interactions with the SACCON apex vortex. The location of the outer vortex separation also fundamentally affects the outer vortex strength and, hence, any manifestations of vortex breakdown. As such, successful modeling/prediction of the blunt-leading-edge vortex would be a prerequisite to modeling of other SACCON-relevant vortex phenomena (e.g., vortex interactions or vortex breakdown) and their associated aerodynamic effects.



a)  $\alpha = 16.83^\circ$       b)  $\alpha = 17.89^\circ$   
**Figure 3. Complex SACCON vortex flow phenomena. USM3D/SA,  $M = 0.15$ ,  $R_{\text{cref}} = 1.61 \times 10^6$ . Frink<sup>16</sup> [2010].**

## B. Conceptual and CFD-Based Aerodynamic Design – Steady Flows

The philosophy for the research wing development was to design a combined-unit (also referred to as a component problem) or possibly a unit problem, along the lines of hierarchy complexity decomposition described by Luckring and Boelens<sup>4</sup> [2015], that would be relevant to the SACCON configuration and isolate as much as possible the selected flow phenomenon, blunt-leading-edge vortical separation onset and progression. The overarching principles for this development were (i) to simulate the leading-edge characteristics of the SACCON configuration, (ii) to keep the research wing as simple as possible, and (iii) to perform CFD sensitivity studies to guide the configuration development. The outcome of this activity was the AVT-183 diamond wing, and details of this process follow.

### 1. Conceptual Design

Leading-edge sweep has a dominant effect on separation-induced vortex flows, as discussed by Hemsch and Luckring<sup>18</sup> [1990]. Much of the knowledge for these vortex flows is anchored in slender wing aerodynamics, but practical UCAV design considerations often result in much lower leading-edge sweep values as compared to slender wings. Such is the case for the SACCON configuration, and it was decided to match the SACCON leading-edge sweep ( $\Lambda_{\text{le}} = 53^\circ$ ) for the research wing. Leading-edge radius also has a dominant role in leading-edge separation, and it was decided to seek values that would be of the same order of magnitude as the SACCON wing ( $r_{\text{le}}/c_{\text{ref}} \sim 0.23\%$ ) and that would diminish in the spanwise direction to further mimic SACCON leading-edge characteristics.

The abrupt changes in trailing-edge sweep for the SACCON configuration can contribute to abrupt changes in span load and hence potentially affect leading-edge separation in a planform specific manner. In keeping with the unit-problem nature of this investigation, it was decided to simplify the trailing edge for the proposed research wing. The simplest trailing edge would be straight, and to keep the overall lower aspect ratio feature of SACCON, it was decided to replace the more complicated SACCON trailing edge with a swept-forward straight trailing edge, resulting in a diamond planform. This would be the simplest planform shape from which CFD sensitivity assessments (including trailing-edge sweep effects) could be performed. The diamond wing could also have testing

advantages for the anticipated wind tunnel model (e.g., small aeroelastic deflections, good internal volume for instrumentation, etc.). The resultant planform is shown in **Figure 4**, with the trailing-edge sweep set equal to half the leading-edge sweep.

With the simple diamond planform, a constant airfoil section would mimic the SACCON spanwise trends of thickness and leading-edge radius and further contribute to the ‘keep-it-simple’ philosophy for the wing. The NACA 64A0xx family of airfoils is still relevant to military aerodynamics, and was chosen as the starting point for CFD sensitivity analysis. It was further decided to start the CFD assessments for a wing with no twist and camber. Polhamus<sup>19</sup> [1996] showed that angle-of-attack loading dominates the blunt-leading-edge separation process, and in addition a planar wing would generate the desired flows at low to moderate angles of attack where experimental flow quality is better and flow field measurements can be simpler as compared to high angle-of-attack conditions. This established what the authors felt would be the simplest possible wing for the CFD assessment studies to be performed. The simple shape would also help with wind tunnel model fabrication.

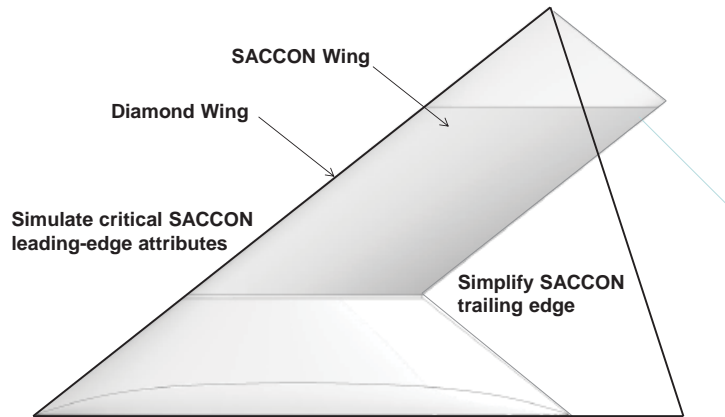
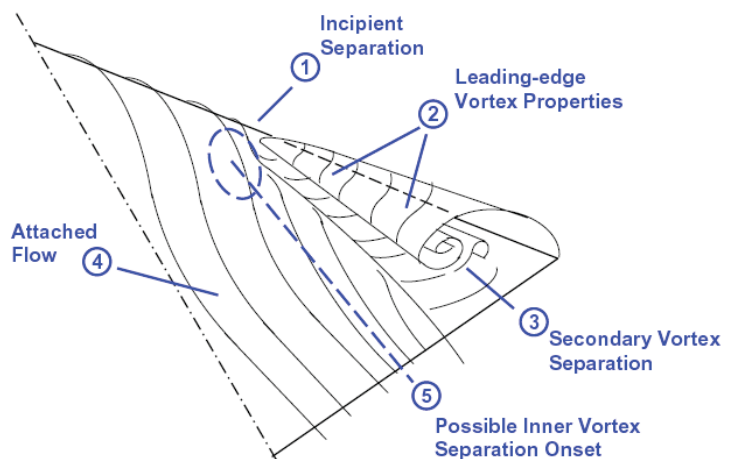


**Figure 4. Diamond/SACCON concept.**

$$\Lambda_{le} = 53^\circ, \Lambda_{te} = -26.5^\circ$$

The aerodynamic objective of this design is to isolate, as much as possible, the separation-induced blunt-leading-edge vortical flow from the many complexities realized on the SACCON model. The conceptual flow field, and critical measurement regions, is shown in the sketch of **Figure 5**. This would represent the simplest possible vortical flow field. The sketch shows an isolated blunt-leading-edge vortex separation for the notional  $53^\circ$  swept diamond wing, and identifies five flow phenomena and measurement regions.

The first phenomenon is incipient separation where a better understanding of the separation onset properties is sought. The second phenomenon is the blunt-leading-edge vortex itself, and two longitudinal measurement stations are included. Because of the blunt edge and low sweep, the properties of this vortex will be different from those known in association with the slender sharp-edged delta wing. The third phenomenon is the secondary vortex, which affects primary vortex attributes. The primary vortex measurement regions would include measurements of the secondary vortex. Finally, the fourth phenomenon is the attached flow on the inboard portion of the wing.



*Note: turbulence representation must model the physics for all phenomena*

**Figure 5. Sketch of flow features.**

Blunt-leading-edge vortex separation can also spawn a small, additional inner vortex from the incipient separation region. Much less is known about this vortex, but it represents a possible fifth flow phenomenon for investigation. It has only recently been researched as part of a recent RTO project, AVT-113<sup>20</sup> [2009], which included blunt-leading-edge vortical studies for a  $65^\circ$  delta wing, Vortex Flow Experiment 2 (VFE-2).

It must be observed that any turbulence model must be able to simulate the flow physics of all these phenomena just discussed. The initial diamond-wing configuration and these flow field characteristics served as the starting point for detailed CFD-based sensitivity analyses.

## 2. CFD-Based Sensitivity Analysis

CFD analyses, including sensitivity effects, were performed to determine if the diamond wing would produce the desired blunt-leading-edge vortical separation. Primary configuration parametric trends were assessed with the block-structured RANS code ENSOLV, which is part of the simulation system ENFLOW (Boerstoel<sup>21</sup> et al. [1996]) from the NLR. A smaller number of assessments were performed with the unstructured RANS code USM3D (Frink<sup>17</sup> [1992]) from NASA LaRC. From a testing perspective, conditions were sought for the incipient separation to occur at about mid length down the leading edge at a low-to-moderate angle of attack. Initial numerical modeling was based upon the Vortex Flow Experiment 2 experiences gained in the RTO AVT-113 project<sup>20</sup>.

The sensitivity studies emphasized airfoil thickness and leading-edge radius effects per the NACA 64A0xx family of airfoils and included angle-of-attack effects. The leading-edge sweep was held at 53° to match the SACCON configuration. Trailing-edge sweep effects were found to be small, and the trailing-edge sweep was held at half the leading-edge sweep,  $\Lambda_{te} = -26.5^\circ$ .

Atmospheric low-speed wind tunnel testing was anticipated, and the sensitivity studies were performed at  $M = 0.2$  and a Reynolds number  $R_{mac} = 3 \times 10^6$ . Selected results from the sensitivity studies follow.

Three profiles were used for the airfoil sensitivity assessments, a NACA 64A010, NACA 64A008, and NACA 64A006. These profiles are shown in **Figure 6**. The airfoils have leading-edge radii, in percent chord, of 0.687, 0.439, and 0.246 respectively, and the variation of leading-edge radius with airfoil thickness for the 64A0xx family of airfoils is shown in **Figure 7**.

For the CFD simulations with ENSOLV, the trailing edge of these profiles was closed by replacing the last one percent of the chord by a quadratic curve. Based on these profiles a diamond wing with a nominal root chord of one meter was constructed. Next a structured multi-block grid, consisting of 56 blocks and about 3 million grid cells, was generated around the diamond wing using NLR's in-house grid generation tools. Though being relatively coarse, this grid was judged sufficient to obtain a first estimate of the separation behavior of the different wings.

For all three wings, an angle-of-attack sweep was performed in 1° increments between 0° and 20°. The ENSOLV simulations were run in fully turbulent mode employing the TNT  $k-\omega$  turbulence model and 1500 cycles were typically sufficient to produce converged results with a three-order drop of residuals.

Results for the three wing thickness at a fixed angle of attack of 12° are shown in **Figure 8**. The results in this figure, as well as in similar figures that follow, are displayed with surface contours of the static pressure coefficient and off-body contours of the x-component of vorticity. They show starboard semispan, viewed from aft and above. These simulations showed that at an angle of attack of 12° only the NACA 64A006 exhibits the desired flow separation at about half way down the wing leading edge. The thicker wings required higher angles of attack for this to occur. This airfoil has the closest leading-edge radius ( $r_{le}/c = 0.246\%$ ) to corresponding values for the outboard portion of the SACCON wing ( $r_{le}/c_{ref} < 0.23\%$ ). From an experimental perspective, angles of attack around 10° were being considered for detailed testing.

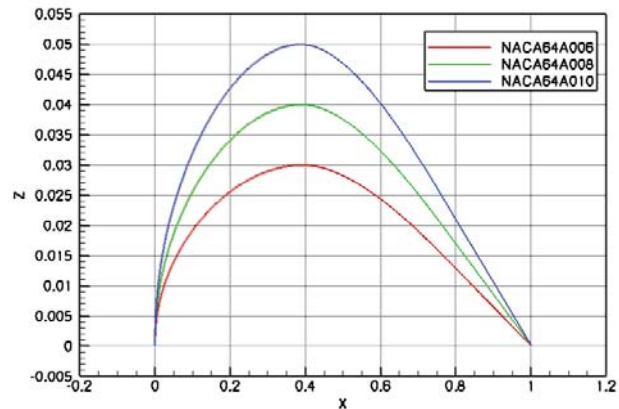


**Figure 6. 64A0xx airfoil sections.**

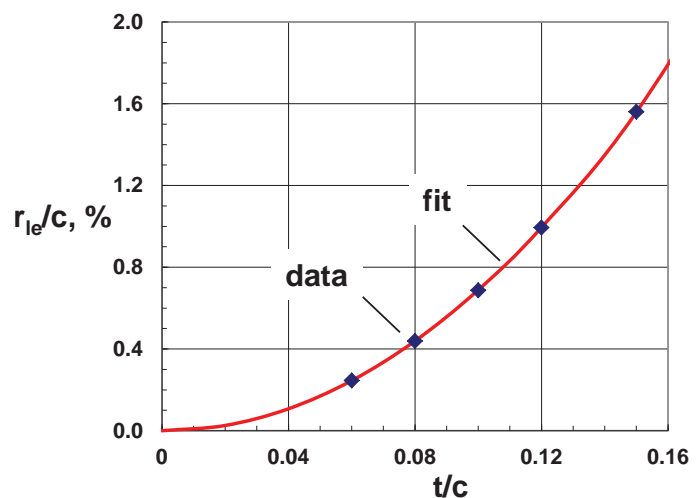
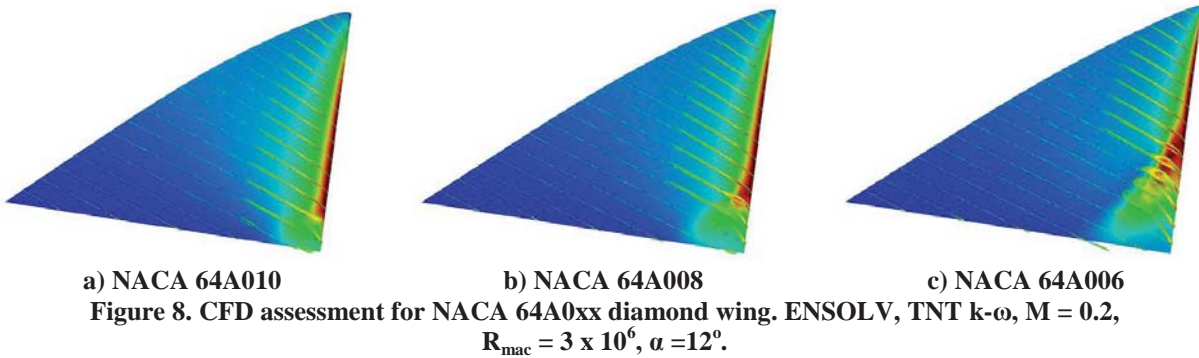
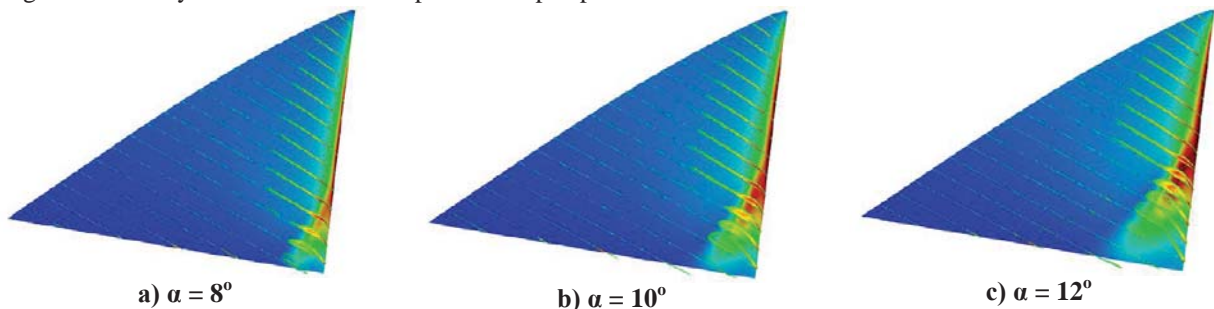


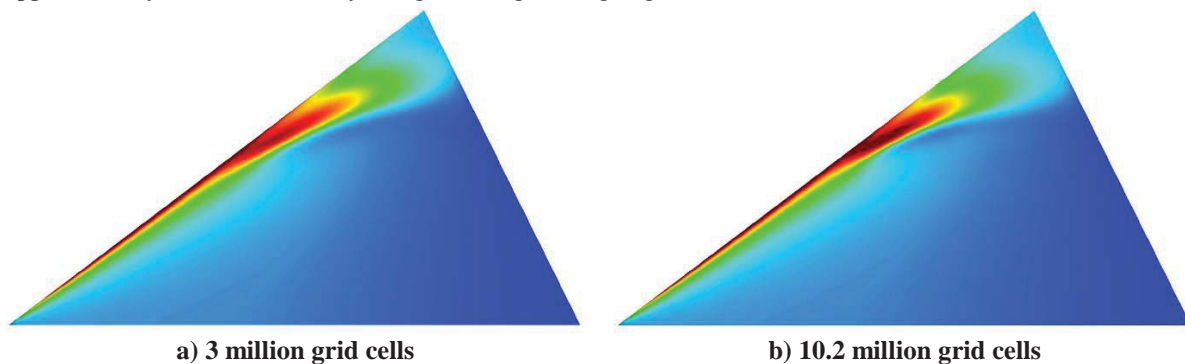
**Figure 7. 64A0xx leading-edge radii.**



Angle of attack effects for the diamond wing with the NACA 64A006 airfoil are shown in **Figure 9** for several angles of attack at the nominal target flow conditions,  $M = 0.2$  and  $R_{mac} = 3 \times 10^6$ . The results show that the desired flow phenomenon, the onset and progression of blunt-leading-edge vortical separation, has been achieved. In addition, the results show a fairly smooth progression of this separation with angle of attack. This smooth progression is very desirable from an experimental perspective.



Grid sensitivity analysis was also performed. The grid dimensions in all directions were multiplied by 1.5, and the resulting grid consisted of 10.2 million grid cells. Both results on the original and fine grid are shown in **Figure 10**. In these images the flow is from left to right. Although the surface pressure coefficient on the fine mesh shows a higher suction peak underneath the vortex and also a more detailed signature, the separation location is approximately the same (halfway along the wing leading edge).



The results of these investigations led to the selection of a NACA 64A006 airfoil with a diamond wing planform that matched the SACCON leading-edge sweep angle ( $53^\circ$ ) and had half that value for the trailing-edge sweep angle ( $-26.5^\circ$ ).

A smaller number of independent computations were performed with the unstructured RANS solver USM3D. The calculations were focused on the nominal target condition ( $M = 0.2$ ,  $R_{mac} = 3 \times 10^6$ ,  $\alpha = 12^\circ$ ) and included i) a comparison between the structured grid and the unstructured grid results, ii) an assessment to isolate thickness and

leading-edge radius effects on the blunt-leading-edge separation, and iii) an assessment of turbulence model sensitivities. Angle of attack effects were computed with the unstructured method for the NACA 64A006 diamond wing, and these computations produced very similar results of onset and progression for leading-edge vortex separation to those that were just shown.

NACA 64A0xx airfoil leading-edge radius and thickness are coupled, so results shown in Figure 8 include effects of both. A hybrid airfoil was designed with the leading-edge radius of the NACA 64A006 and the thickness of the NACA 64A010 while retaining the overall class of pressure distribution of the NACA 64A0xx airfoils. An unstructured-grid calculation at  $\alpha = 12^\circ$  showed basically similar results to NACA 64A006 unstructured results as well as the structured-grid results of Figure 8. This limited result implied that leading-edge radius is affecting the blunt-leading-edge vortical separation for this diamond wing to a greater degree than airfoil thickness. The result also demonstrated that if additional thickness were needed, say from a model manufacturing or instrumentation perspective, the hybrid airfoil could accommodate this need while retaining the desired leading-edge separation properties.

Finally, three turbulence models (SA, SST, k- $\epsilon$ ) were used with the unstructured method to assess the effect of each on the blunt-leading-edge separation for the diamond wing at the nominal target condition ( $M = 0.2$ ,  $R_{mac} = 3 \times 10^6$ ,  $\alpha = 12^\circ$ ). The results are shown in **Figure 11** from a starboard vantage point with the wing apex to the right. Here surface streamlines are displayed along with off-body contours of the longitudinal vorticity component. This study demonstrated a significant shift in separation onset location around a point about halfway down the wing leading edge; the shift in separation onset due to turbulence model was approximately 11% of the leading-edge length. The diamond wing still retained a sensitivity to turbulence modeling.

It is noteworthy that the flow topology in the incipient separation region of Figure 11 was the first such observed, and considered to be most curious and not well understood. Subsequent research has produced this same overall topology from other CFD methods (see Frink<sup>10</sup> [2015], Hitzel<sup>11</sup> et al. [2015]), and the understanding of the flow is under scrutiny at the time of this paper.

The CFD studies demonstrated that this diamond wing exhibited the desired characteristics for a unit/combined-unit problem connected to the parent SACCON flows. In addition, it was a very simple shape that is easy to define for grid generation or wind tunnel model manufacturing.

The outcome of this work was that it made sense to pursue preliminary design of a wind tunnel model. Preliminary considerations for interfacing the configuration with the facility would be addressed, as well as planning for types of data that could be obtained. Data would be sought that could enhance our understanding of this flow, and thereby enable physics-based CFD modelling for improved predictions of the blunt-leading-edge separation onset and progression.

As steps were being initiated toward a wind tunnel campaign, some brief but advanced unsteady aerodynamic analysis was performed for the diamond wing. This analysis is summarized next.

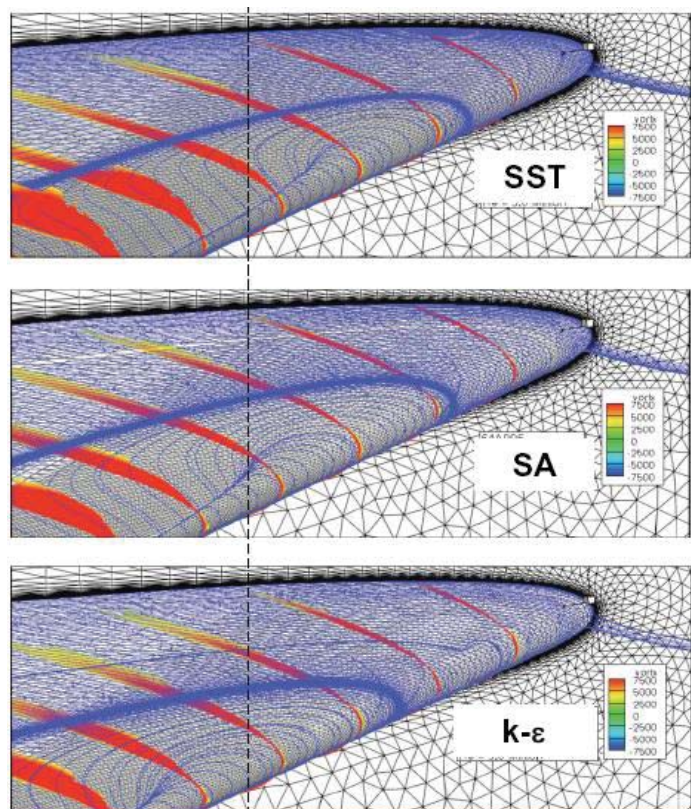


**Figure 11. Turbulence model assessment for NACA 64A006 diamond wing. USM3D,  $M = 0.2$ ,  $R_{mac} = 3 \times 10^6$ ,  $\alpha = 12^\circ$ .**

### C. CFD-Based Aerodynamic Analysis – Unsteady Flow

A preliminary analysis of unsteady aerodynamic effects for the proposed diamond wing configuration was conducted with an advanced zonal detached eddy simulation method, ZDES, as originally proposed by Deck<sup>22</sup> [2012]. The method has only recently been published along with a suite of successful applications over a range of Mach numbers and configurations (see Deck<sup>23</sup> [2012] and Deck<sup>24</sup> et al. [2014]). Because the method is relatively new, some details of the formulation and its application to the diamond wing are included in the appendix of this report. Selected results from that appendix are highlighted in this section.

Block structured grids for the diamond wing were developed with approximately  $18 \times 10^6$  points. The initial planning for the wind tunnel tests included indications for a slightly lower free stream Mach number for the anticipated experiments. The conditions for the unsteady ZDES computations therefore were  $M = 0.15$ ,  $R_{mac} = 2.74 \times 10^6$ , and  $\alpha = 12^\circ$ . Test planning included interests for unsteady surface pressure measurements, and the ZDES results were viewed as a first look at the magnitudes, locations, and spectral content for unsteady pressures and flow fields for this wing.

A sample result of the unsteady vortical flow predictions from ZDES is shown in **Figure 12**. Here the unsteady vortical structures are illustrated with the Q-criterion,  $Q = \frac{1}{2}(\|\Omega\| - \|S\|)$ , where  $S$  and  $\Omega$  denote the strain and rotation tensors, respectively, and vortex tubes correspond to positive values of  $Q$ . Vortical structures are coloured by the non-dimensional streamwise velocity, and total pressure loss is shown in a downstream plane. The results also clearly show both the leading-edge primary vortex as well as the smaller co-rotating inner vortex.

Unsteady surface pressure coefficients,  $C_{p,rms}$ , are shown in **Figure 13** from the ZDES predictions. In this figure, the flow is from right to left. Primary unsteadiness is concentrated under the vortical separation with very little inboard influence. The results also demonstrate that the onset of unsteadiness appear to coincide with the incipient vortical separation. It is also observed that the incipient separation location is roughly at the mid-leading-edge location in the unsteady ZDES results, similar to the steady ENSOLV and USM3D results. This would imply that the unsteadiness, at least to first order, is not affecting the incipient separation location very much. More detailed analysis of the unsteady effects on the separation onset details would be of interest.

These results provided initial guidance for unsteady pressure characteristics associated with the specific wing under study. Additional unsteady analysis with OVERFLOW2 (Trammel<sup>25</sup> et al. [2009]), combined with the ZDES results, guided the sizing and placement of unsteady surface pressure measurement transducers. The reader is referred to the ZDES appendix for a brief discussion of the method and more detailed presentation and analysis of the ZDES results, including those highlighted here.

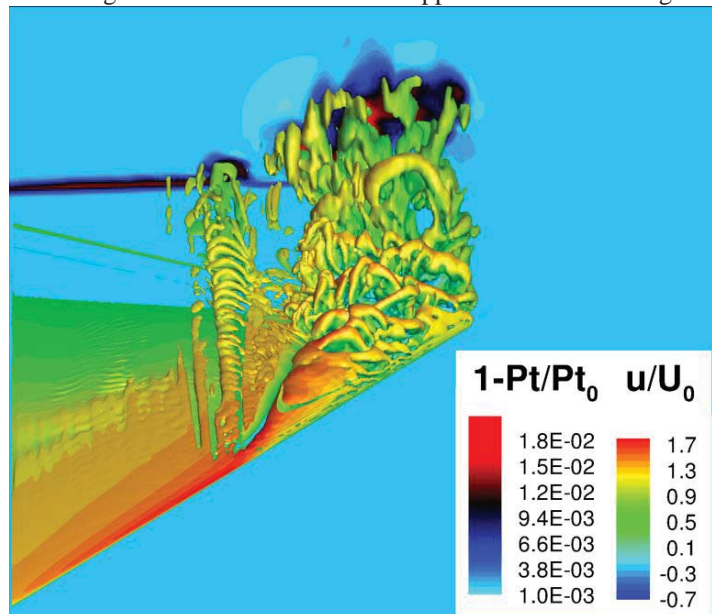


**Figure 12. Turbulent vortex structures.**  
 $M = 0.15$ ,  $R_{mac} = 2.74 \times 10^6$ ,  $\alpha = 12^\circ$ .

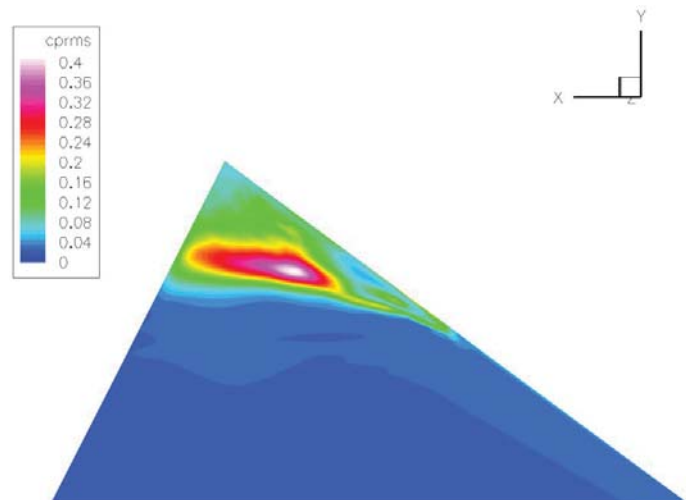


**Figure 13. Surface unsteady pressure coefficient contours,**  
 $C_{p,rms}$ .  $M = 0.15$ ,  $R_{mac} = 2.74 \times 10^6$ ,  $\alpha = 12^\circ$ .

#### IV. Model Development

Broad characteristics of the diamond wing had been established from the computational studies including nominal focus conditions for the blunt-leading-edge vortex separation to occur. With the basic flow established on the diamond wing, steps were taken to develop a realizable wind tunnel model suitable for testing. Wind tunnel model development can only be done in the context of the experimental facility, so facility related impacts to the model had to be addressed. In this section, facility characteristics will first be addressed followed by mechanical and instrumentation aspects of the wind tunnel model. Computer aided design and manufacturing considerations are also addressed.

##### A. Wind Tunnel Facility Characteristics

Within the early design phase of AVT-183, the Institute of Aerodynamics and Fluid Mechanics of the Technical University, Munich (TUM-AER) agreed to perform experimental investigations, thus contributing to the task group. For this reason, the design process of the present diamond wing configuration was also driven by wind tunnel facility requirements of TUM-AER. General characteristics of the facility are reviewed, followed by some impacts to the wind tunnel model.

Wind tunnel facility A was identified for the AVT-183 diamond wing experiments and a drawing of this facility is shown in **Figure 14**. The facility is a closed-circuit, single return low-speed wind tunnel with a test section that can be used in either a closed (solid-wall) or an open (floor only) configuration. The facility has a well-recognized capability for detailed flow field measurements, surface pressure measurements, and force and moment testing. Some overall characteristics of the facility are summarized in **Table 1**. The detailed flow field measurement capability requires, for the most part, the open test section configuration.

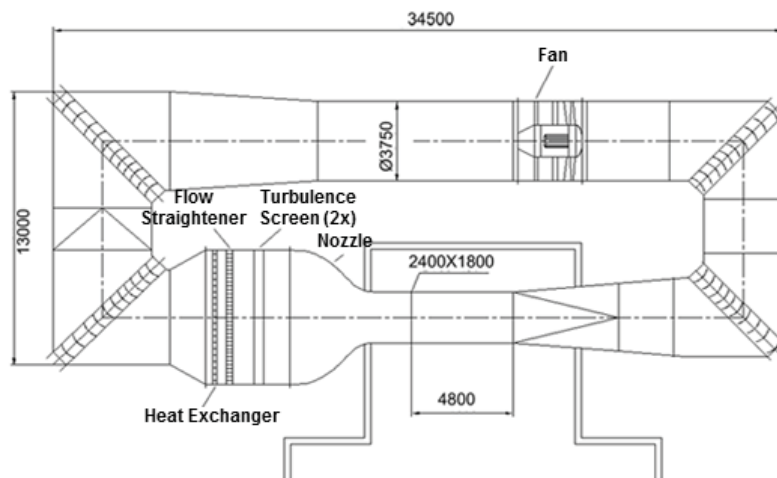


**Figure 14. Wind tunnel facility A at TUM-AER. Dimensions shown in millimeters.**

**Table 1. Characteristic data of the wind tunnel facility A at TUM-AER.**

Characteristic data (open/closed)		Quality of flow (open/closed)	
Cross section of test section	1.80 m x 2.40 m	Turbulence intensity	$Tu_x = Tu_y = Tu_z < 0.4\% / < 0.2\%$
Contraction ratio	7 : 1	Angle divergence	$\Delta\alpha = \Delta\beta < 0.20$
Test section length	4.80 m	Static pressure deviation	$\Delta p/q_\infty \leq 0.4\%$
Maximum power	420 kw	Temporal speed non-uniformity $x = 1.5m, r_{ts} \leq 0.8m$	$U_\infty \leq 20m/s: \Delta U_\infty \leq 0.12m/s$ $U_\infty > 20m/s: \Delta U_\infty \leq 0.0067 U_\infty$
Maximum velocity	65 / 75 m/s	Spatial speed non-uniformity $x = 1.5m, r_{ts} \leq 0.8m$	$U_\infty \leq 20m/s: \Delta U_\infty \leq 0.12m/s$ $U_\infty > 20m/s: \Delta U_\infty \leq 0.0067 U_\infty$
		Reynolds number (10% blockage)	$2.77 \times 10^6$

Flow field data were critical to the planned experimentation, and therefore the open test section configuration was selected for the experimental work. In this configuration, the experiments could be performed with a semispan model, and for the test section size of the facility, this created an opportunity to increase the size of the model from the nominal value used in the CFD studies ( $c_r = 1.0m$ ). Among other considerations, the larger model was attractive for flow field measurement resolution, surface pressure measurement resolution, and internal instrumentation needs. The open test section also has a lower free stream maximum speed, below  $M=0.2$  of the preceding CFD analysis. A highest low-speed Mach number was desired from a CFD convergence perspective as well as from the interest to have the highest Reynolds number possible. When balanced with facility operations and data quality considerations,

a reduced Mach number of 0.15 was chosen. With an increased model root chord of 1.2m, this would result in an experimental Reynolds number, based on mean aerodynamic chord, of  $2.7 \times 10^6$ , fairly close to the Reynolds number used in the CFD studies ( $3 \times 10^6$ ). These modified test conditions seemed close enough to those of the CFD design studies so that the CFD results would still be applicable to the experiments. Some other consequences of the open test section testing will be discussed in Section V, Experiment Development.

One consequence of the semispan testing is that the diamond wing would need to be mounted on a peniche (i.e., standoff) to mitigate influences from the boundary layer on the floor of the wind tunnel. Benchmark data for the floor boundary layer are available, and an example is shown in **Figure 15**. Measured boundary layer profiles are shown in tunnel coordinates for a number of longitudinal stations down the centerline of the tunnel floor in the test section, and an approximate boundary layer thickness of 50mm is indicated. Based on prior wind tunnel testing experiences, a best-practices peniche height of 90mm was selected for the present investigations. This peniche height corresponds to  $0.075 c_r$ . For this case, minimal influence of the wind tunnel floor should be observed on the flow around the wind tunnel model. Assessments for any peniche effects are presented in the next section.

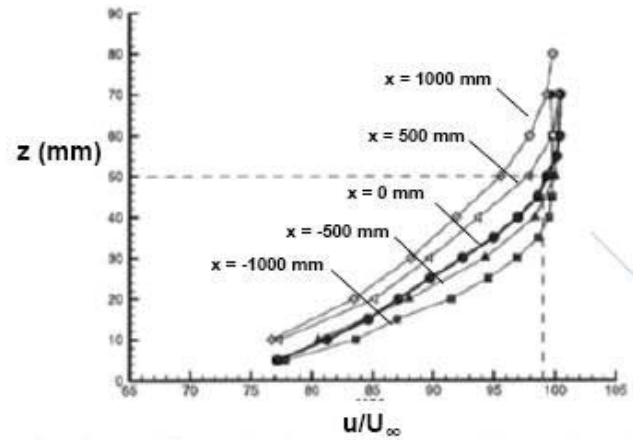


**Figure 15. Floor boundary layer profiles.**  
 $U_\infty = 60 \text{ m/s}$ , Wind tunnel facility A, TUM-AER.

## B. Model

From a facility interface perspective the diamond wing had now been sized to a root chord of 1.2m and a wing semispan of approximately 0.657m to stand on a peniche of 0.090m. The following sections address the initial mechanical design of the model, instrumentation layout, and final design. Once again, CFD was used extensively in guiding this work.

### 1. Initial Mechanical Design

Effects of the peniche were assessed with CFD to determine any consequences of the peniche-wall interface flow on the diamond wing onset and progression of blunt-leading-edge separation. Additional simulations were performed for the wind tunnel model ( $c_r = 1.2\text{m}$ ) with the block-structured solver ENSOLV. These simulations included the peniche and wind tunnel floor boundary layers to integrate the model with the wind tunnel environment. An entrance length of  $2c_r = 2.4\text{m}$  was sufficient to approximate the floor boundary layer thickness. The grid consisted of 134 blocks and 13.5 million grid cells. Simulations were performed for the expected wind tunnel conditions (i.e.,  $M = 0.15$  and  $R_{mac} = 2.7 \times 10^6$ ). These simulations were run in fully turbulent mode employing the EARSM turbulence model.

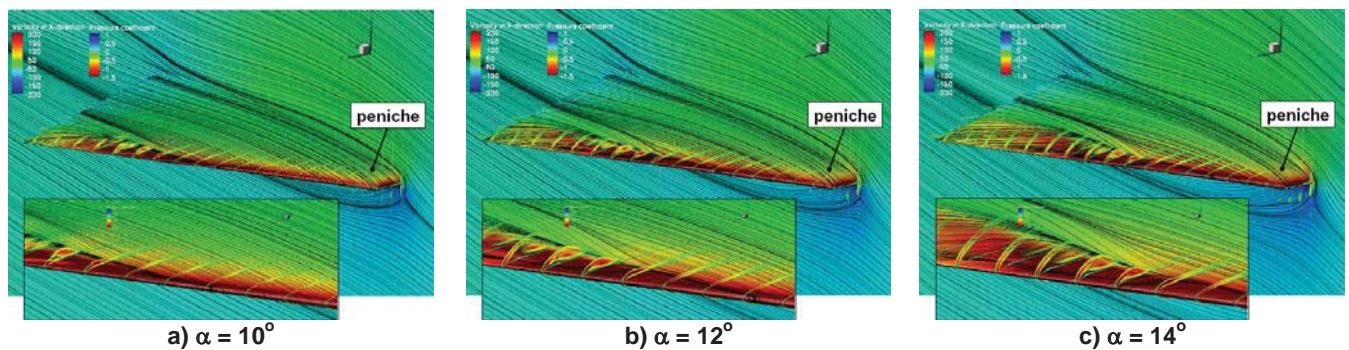


**Figure 16. CFD assessment for NACA64A006 diamond wing ( $c_r = 1.2\text{m}$ ) including peniche (peniche height =  $0.090\text{m} = 0.075 c_r$ ). ENSOLV, EARSM,  $M = 0.15$ ,  $R_{mac} = 2.7 \times 10^6$ .**

Angle of attack sensitivities for this geometry are shown in **Figure 16**. In these images, the flow is from right to left. These results demonstrate once more a smooth progression of the leading-edge separation with angle of attack.

In addition, at  $\alpha = 12^\circ$  the separation still appears to be near the mid-span of the wing. These simulations also show that the horseshoe vortex at the wall/peniche intersection is limited to a small region and thus, does not significantly influence the flow over the wing. Based on these results, and the best practices from the facility, the recommended peniche was accepted for the planned experiments.

CFD loads were used for guiding the basic mechanical design of the model, and the loads were small compared to capabilities from conventional metal materials. The 6% thick airfoil was acceptable from this perspective, and would be further assessed during instrumentation layout assessments.

Although all the AVT-183 wind tunnel experiments for this diamond wing were planned for low speeds at wind tunnel facility A of TUM-AER, the wind tunnel model was further designed for more demanding wind tunnel test conditions. This design would enable operation under cryogenic wind tunnel conditions as well, applying considerably higher dynamic pressures and/or modified ambient conditions (temperature, pressure) in future analyses with the diamond wing wind tunnel model. For this reason, the aluminum alloy CERTAL (AlZn5Mg3Cu) was chosen as the material to be used. It offers a tensile strength about 35% higher than comparable aluminum alloys, which is favorable for the cryogenic high-load testing environment. In addition, the necessary bolted connections of the wind tunnel model were designed for considerably higher loads than needed for operation in the wind tunnel facility of TUM-AER. A side benefit to this material used for the diamond wing is that aeroelastic deformations in the tests at TUM-AER could be expected to be extremely small.

## 2. Detailed Instrumentation Development

Locations for the detailed surface pressure measurements (steady and unsteady) were guided extensively from CFD. The same target conditions ( $M = 0.15$ ,  $R_{mac} = 2.7 \times 10^6$ ,  $\alpha = 12^\circ$ ) were retained for this assessment but now for the CFD simulation including the peniche. A conical slender-wing approach was taken for the surface pressure tap locations, although special attention was needed due to vortex separation occurring about midway down the leading edge and incipient separation effects extending upstream of this location. Tradeoffs had to be made between pressure interests from a CFD perspective and pressure measurements that could be realized from a wind tunnel model perspective (e.g., internal space requirements, accessibility, manufacturing).

One key step in these tradeoffs was to sample the high spatial fidelity CFD solutions at the discrete locations being considered for the wind tunnel model pressure taps. An example for this analysis is shown in **Figure 17**, which also illustrates the final static surface tap locations. (Kulite<sup>®</sup> information on this figure will be discussed later.) The work was done with the NLR flow solver ENSOLV, and illustrates that for the discrete locations chosen, clear indications can be found of attached flow, incipient separation, and vortical flow. The figure also shows a

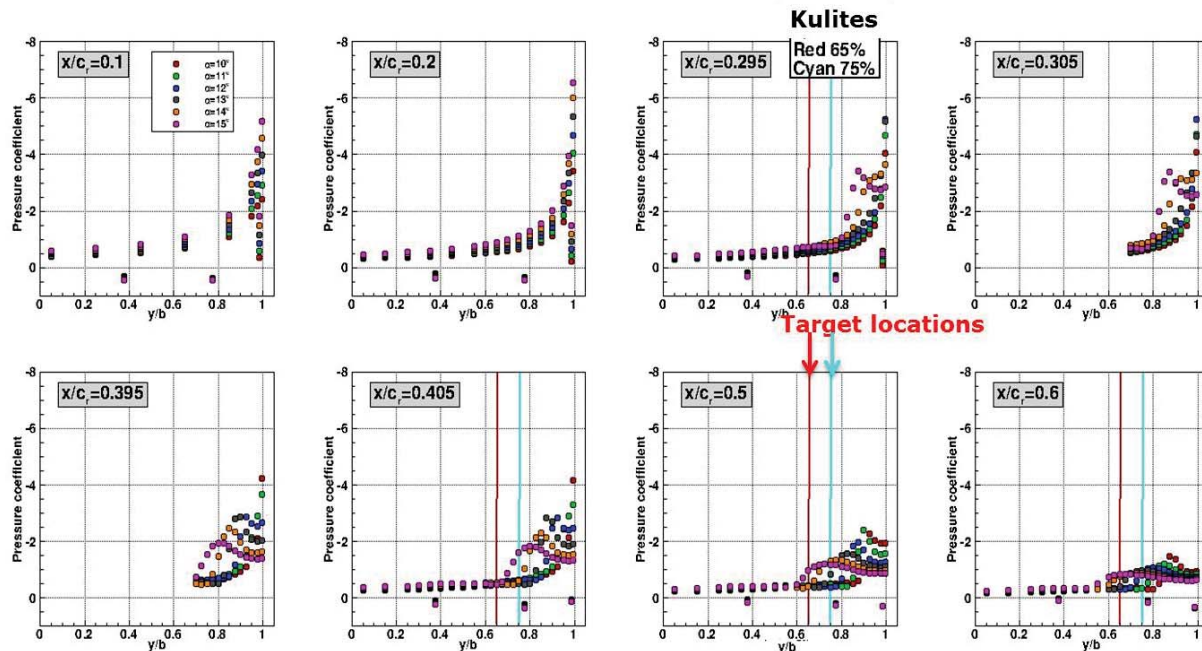


**Figure 17. Steady and unsteady pressure locations, NLR  $C_p$  predictions.**  
 $M = 0.15$ ,  $R_{mac} = 2.7 \times 10^6$ ,  $\alpha = 10, 11, 12, 13, 14$ , and  $15^\circ$ .

doubling of the longitudinal stations around  $x/c_r \approx 0.3$  and  $x/c_r \approx 0.4$  where separation onset is expected. Part of the reasoning for this finer resolution was that fine angle-of-attack adjustments could be made during the experiments to move the incipient separation through this region.

For this final layout, eight chord-wise sections were defined for the surface pressure taps. A total of 145 pressure taps are located on the suction side shell (eight with Kulites), and 17 additional pressure taps are located on the pressure side shell. The peniche is also instrumented with 9 static pressure taps.

For the conventional static surface pressure taps only time-averaged steady surface pressure measurements are undertaken, whereas for the eight Kulite sensors record time-dependent data can be obtained as well. The location of the Kulites required additional analysis from unsteady CFD simulations, and these locations were established after the steady-state static surface pressure tap locations on the wing upper surface and peniche were finalized. The steady CFD predictions from NLR were used in conjunction with unsteady predictions by ONERA (see Section III-C and Appendix A) along with new AEDC computations using the OVERFLOW2 code (see Trammel<sup>25</sup> et al. [2009]) to finalize the location of the eight Kulite pressure measurements. All unsteady taps were planned for the upper surface, and unsteady predictions by ONERA provided first estimates of the spectral map to evaluate candidate locations for the unsteady measurements. Unsteady AEDC predictions then were used with NLR and ONERA distributions to confirm that the proposed Kulite locations would provide the desired characterization of the unsteady aspects of the complex flow at discrete angles of attack between 10 and 15 degrees. Two rays ( $y/s = 0.65, 0.75$ ) and four longitudinal stations ( $x/c_r = 0.295, 0.405, 0.5, 0.6$ ) were chosen for the final unsteady pressure tap locations as indicated in Figure 17. With these locations, it was felt that an onset and progression of unsteady flow effects with increasing angle of attack might be detected.

The locations of both the steady and the unsteady upper surface pressure taps are super-imposed with the steady CFD results from NLR in **Figure 18** at the target flow conditions for both the wing and the peniche. Additional information about the surface pressure measurements can be obtained from Hövelmann<sup>5</sup> et al. [2015], in which the instrumented wind tunnel model is introduced and explained in detail.

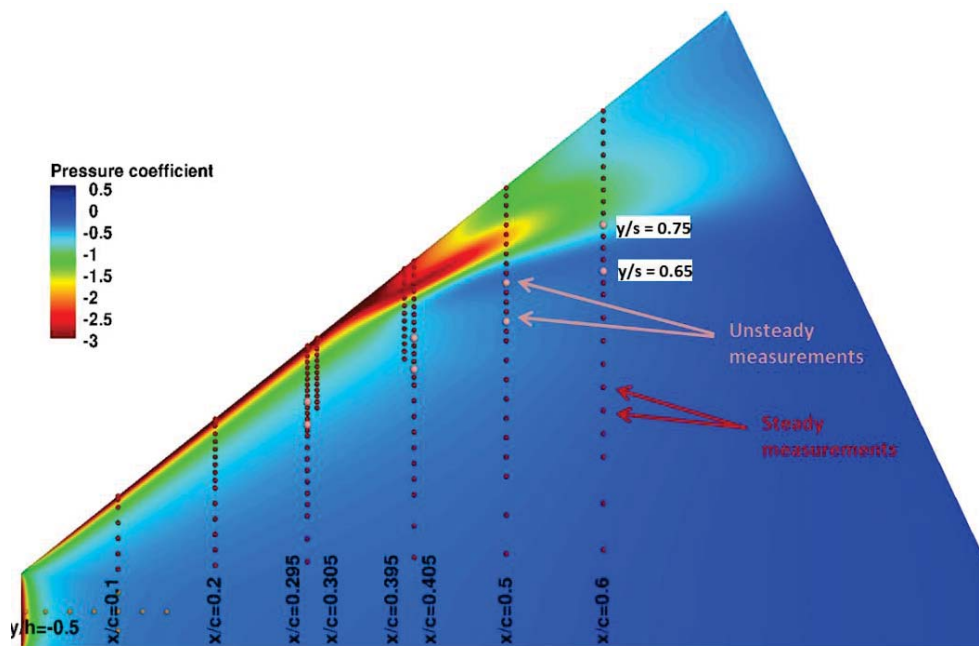


**Figure 18. Steady and unsteady pressure locations on the upper surface of the wing, NLR  $C_p$  predictions.  $M = 0.15, R_{mac} = 2.7 \cdot 10^6, \alpha = 12^\circ$ .**

### 3. Final Model Design and Manufacturing

Based on the final shape and size of the diamond wing configuration from extensive CFD computations and facility considerations, the final wind tunnel model design was performed with Computer Aided Design (CAD) technology. In a first step, the NACA 64A006 profile was applied to different span-wise sections to set up a parametric CAD structure, thus defining the outer shape of the wind tunnel model (see the left plot of **Figure 19**). Next, the necessary parts of the wind tunnel model were defined, resulting in the main suction and pressure side shell and six different leading-edge inserts. The leading-edge inserts were designed for an improved pressure

instrumentation process, since most of the pressure taps are located close to the leading edge, where the available space for the instrumentation is drastically reduced. With the removable inserts, the instrumentation process could be achieved in a sophisticated way. Moreover, the suction and pressure side shell were not divided exactly at the symmetry x-y plane (i.e.,  $z = 0$ ), which would have led to disadvantages at the leading and trailing edges during the manufacturing process. With the chosen fragmentation as shown in the right plot of Figure 19, both the leading and the trailing edges are free from any gaps, since the wind tunnel model partition is moved inward. In order to connect the different parts with each other, suitable bolt connections were defined. Since all bolt connections were placed on the pressure side shell, the suction side shell remained free from any surface deficits.

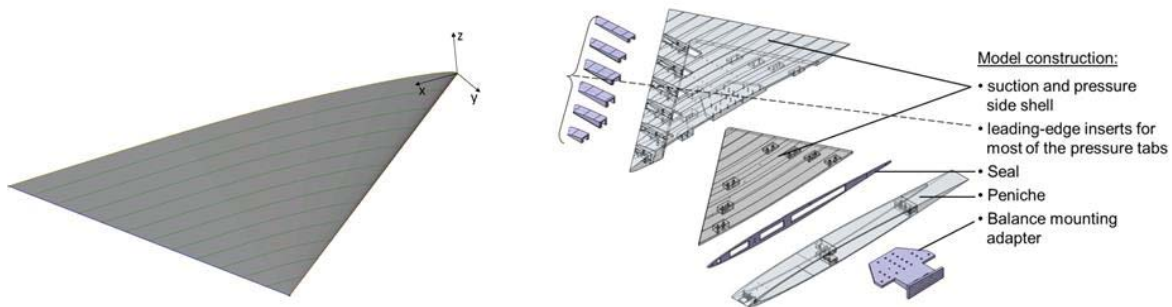


**Figure 19. Parametric CAD surface (left) and overall components of the wind tunnel model (right).**

In addition, the peniche including the seal and the balance mounting adapter were designed to interface with the wind tunnel model as shown on the right side of Figure 19. The height of the peniche was retained ( $h = 0.090\text{m}$ ) as discussed above, and the shape of the peniche was designed to match the root chord airfoil. This shape was extended to the wind tunnel floor with a constant chord and intersected perpendicular to the floor in accordance with best practices at the facility.

Finally, the manufacturing process was conducted based on the CAD design of the wind tunnel model. Three axis milling machines were used to build each of the wind tunnel model components. For example, the left plot of **Figure 20** shows the inner contour of the suction side shell. The outer contour close to the leading and trailing edges as introduced above is noticed as well. Subsequent to the rough-milling process, the components were assembled.



**Figure 20. Milling of the wind tunnel model (left) and surface accuracy measurements (right).**

Hence, the fine-milling was performed on the complete wind tunnel model, in order to avoid discontinuities of the surface contour between the different components of the wind tunnel model. The orifices of the pressure taps (diameter  $d = 0.3\text{mm}$ ) were then drilled into the wind tunnel model. All pressure taps are aligned normal to the wing surface contour. After the milling process, the surface contour accuracy was measured in detail (see Figure 20, right side) and compared to the given CAD data. The geometrical similarity of the wind tunnel model and the wing surface geometry representative for the numerical analyses could thus be verified.

## V. Experiment Development

The objectives for this experiment are focused on increasing our understanding of the vortical flows that occur on moderately swept and blunt leading edges for moderate aspect ratio wings pertinent to UCAV configurations, and to do so in a way that could lead to improved predictive capability from CFD methods. This is a class of leading-edge vortex flow that is not as well documented or understood as the leading-edge vortices that form on slender, sharp-edged delta wings. Many details of the new experiments will be reported by Hövelmann<sup>5,6</sup> et al. [2015], but some overarching principles are worth summarizing in this report.

The model was purposely designed to be simple and to isolate as much as possible the particular flow phenomenon of interest, to perhaps represent a unit or combined-unit class of problem, and as such, the test program was informed to a large degree by CFD validation testing principles. A number of these guidelines could be implemented in the program; others could not.

Multiple entries for the experimental campaign were planned and these entries have provided for short-term, mid-term, and long-term uncertainty quantification in the measurements. Both global properties and local flow physics characteristics were measured, and multiple measurement techniques were used. These included force and moment measurements from an external strain-gauge balance, static and dynamic surface pressure measurements, and detailed flow-field measurements for all three mean and fluctuating velocity components. Flow field measurements were obtained with two independent techniques, stereo Particle Image Velocimetry (PIV) and hot-wire probes. Test section flow characterization measurements were also obtained. The facility already had a good overall characterization (see Table 1) from prior work as well as additional information such as floor boundary layer profiles. In the course of the diamond wing entries, this information was extended to include inflow plane characterization and some pseudo far-field characteristics, both from hot-wire measurements.

The pseudo far-field measurements were a compromise between the requirement to test in an open test section for flow-field quantification and the need to have far field boundary conditions quantified from the experiment for CFD simulations. Solid walls with quantified aerodynamic wall properties are generally desired from a validation perspective. The pseudo far field measurements in the current work were obtained with hot-wire probes along longitudinal traces above, below, and outboard of the wing, and do not meet the expectations for validation-class testing. However, it was felt that the far field information, in conjunction with the rest of the measurement campaign, could provide useful data to help discriminate among various CFD codes as to their modeling of the subject flow. For example, the flow physics measurements in the leading-edge primary and secondary vortices could provide guidance toward the adequacy for these vortex simulations from various turbulence model implementations.

## VI. Concluding Remarks

A diamond wing model has been designed to isolate as much as possible the onset and progression of blunt-leading-edge vortex separation from a moderately swept leading edge. The wing represents a unit, or perhaps combined-unit problem relevant to a more complex UCAV configuration known as SACCON. CFD was extensively used to both develop the wing with the desired flow properties and to guide wind tunnel model considerations such as instrumentation layout and facility interface effects. Steady and unsteady aerodynamic effects were included in the study.

Test planning for this wing includes a fairly comprehensive set of measurements. These include global force and moment properties, static and dynamic surface pressure distributions, and mean and fluctuating flow field properties in the vortical flows. In addition, the plan includes characterization of many test section flow features. The tests have recently been completed and will be the subject of subsequent publications. Numerous CFD assessments of the blunt-leading-edge vortical flows that use these data have also been recently completed and will be the subject of subsequent publications.

## VII. Acknowledgments

The work was part of a NATO/STO program entitled “Reliable Prediction of Separated Flow Onset and Progression for Air and Sea Vehicles”, also known as AVT-183. The authors appreciate the opportunity to work within the Applied Vehicle Technology (AVT) sector of the STO.

The work has been supported by a number of program and project offices. These include the NASA Aerospace Sciences (AS) and the Environmentally Responsible Aircraft (ERA) programs, the NLR programmatic research funding “Kennis voor Vermogen”, and the French Aerospace Laboratory ONERA. All of this support is appreciated. In addition to the authors, the AEDC CFD analysis was performed by William Sickles and Derick Daniel, and the authors appreciate their contributions.

## VIII. Appendix A – Details of ZDES Numerical Method and Diamond Wing Analysis

As the need for higher accuracy simulations has increased, the computational fluid dynamics (CFD) community has in turn put emphasis on assessing the quality of the results and now focuses a great deal of its effort on validation of advanced methods. Let us remember that the validation of inviscid calculations was primarily focused on the capability to evaluate the wall pressure distribution while the validation of steady viscous calculations was mainly based on the correct assessment of the boundary layer integral quantities. Now the flow-field model has to include a comprehensive unsteady description of turbulence including fluctuations both in pressure and velocities (see the discussion by Sagaut and Deck<sup>26</sup> [2009]).

In the framework of AVT-183, one of the objectives of this preliminary unsteady simulation is precisely to get a first insight into the spatial organization of the fluctuating aerodynamic field. Especially, such knowledge may help the experimentalist in the location of the unsteady Kulite sensors and permits to get an idea of the frequencies of interest.

This section is organized as follows. The salient features of the unsteady calculation including the ZDES approach as well as the computational description are first briefly presented before getting interested in the Reynolds-averaged data and in the fluctuating pressure and velocity fields.

### A. Zonal Detached Eddy Simulation (ZDES)

The ZDES was first proposed by Deck<sup>22</sup> [2012] and the complete formulation has been recently published by Deck<sup>23</sup> [2012]. This method belongs to the family of multiresolution approaches and is initially based on the Spalart-Allmaras (SA) RANS model<sup>27</sup> but can be extended to any eddy viscosity model.

This approach takes full advantage of its zonal nature, not only to allow the user to specify RANS and LES regions, but also to make possible the use of various formulations within the same calculation. Besides, the ZDES also provides an ‘automatic’ operating option (referred to as mode 2 in the following) for which the switch between RANS and LES regions is dynamically set by the model itself. Thus, ZDES offers an attractive flexibility in the treatment of turbulent flows in technical applications and has been applied often with good results over a range of Mach numbers and configurations (see Deck<sup>23</sup> [2012], Deck<sup>24</sup> et al. [2014]). To guide the aerodynamicist through the simulation process, a system based around flow taxonomies is proposed in the framework of ZDES.

Indeed, three specific hybrid length scale formulations (see Equation (A-1)), also called modes, are optimized to be employed on three typical flow field topologies as illustrated in **Figure A-1**. Mode 1 concerns flows where the separation is triggered by a relatively abrupt variation in the geometry; mode 2 is retained when the location of separation is induced by a pressure gradient on a gently curved surface, and mode 3 for flows where the separation is strongly influenced by the dynamics of the incoming boundary layer (see Figure A-1). All these flow cases may be treated by the same ZDES technique in its different modes. An example where the three modes of ZDES are used at the same time on a curvilinear geometry can be found in Deck and Larauie<sup>28</sup> [2013].

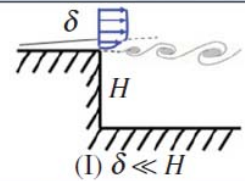
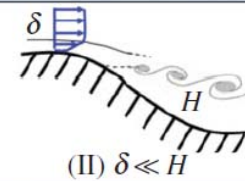
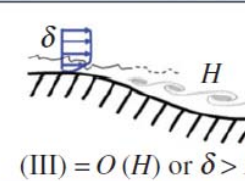
Though the method can be adapted to any turbulence model, in the framework of the underlying SA model<sup>27</sup>,  $d_w$  is replaced with  $\tilde{d}_{ZDES}$  in the model according to:

$$\tilde{d}_{ZDES} = \begin{cases} d_w & \text{if } \text{mode} = 0 \text{ (ie RANS)} \\ \tilde{d}_{DES}^I(\tilde{\Delta}) & \text{if } \text{mode} = 1 \\ \tilde{d}_{DES}^{II}(\tilde{\Delta}) & \text{if } \text{mode} = 2 \\ \tilde{d}_{DES}^{III}(\tilde{\Delta}) & \text{if } \text{mode} = 3 \end{cases} \quad (\text{A-1})$$

where  $\tilde{\Delta}$  is the new length scale entering ZDES. In the framework of ZDES, the proposal of a new subgrid length scale  $\tilde{\Delta}$  is not a minor adjustment of the detached eddy simulation (DES) formulation, because the modified length scales depend not only on the grid ( $\Delta x, \Delta y, \Delta z$ ) as in DDES<sup>29</sup>, but also on the velocity gradients ( $U_{i,j}$ ) and eddy viscosity fields ( $\nu_t$ ), because:

$$\tilde{\Delta} \equiv \tilde{\Delta}(\Delta x, \Delta y, \Delta z, d_w, U_{i,j}, \nu_t) \quad (\text{A-2})$$

In the present case, only mode 2 (i.e., ‘automatic’ mode of ZDES) is retained since the onset of separation is not known a priori on the round leading edge (see Figure A-1).

zonal detached eddy simulation (ZDES)			
	mode 1	mode 2	mode 3
flow category	 (I) $\delta \ll H$	 (II) $\delta \ll H$	 (III) $= O(H)$ or $\delta > H$
applications	base flow, free shear flows, spoilers, steps, slat/flap cove, etc.	buffet, flaps, duct flows, nacelle intake, etc.	corner flows, turbulent boundary layer, separation onset on high-lift devices, shallow separations, etc.

**Figure A-1. Classification of typical flow problems. I: separation fixed by the geometry, II: separation induced by a pressure gradient on a gently curved surface, III: separation strongly influenced by the dynamics of the incoming boundary layer (adapted from Ref [23]).**

### B. Computational Description

A structured multi-block mesh has been designed based on the common CAD file defined by NLR. This grid is made of 40 blocks and is based on a 0-H topology in order to get, as far as possible, square-shaped cells on the wing. The size of the domain is  $[-10 < Lx/c_r < 6] \times [-0.075 < Ly/c_r < 7] \times [-5.5 < Lz/c_r < 5.5]$  ( $c_r = 1.2\text{m}$  is the root chord). The total number of points is  $N_{xyz} = 18 \times 10^6$  points. The extent of the computational domain as well as the surface mesh is depicted in **Figure A-2**.

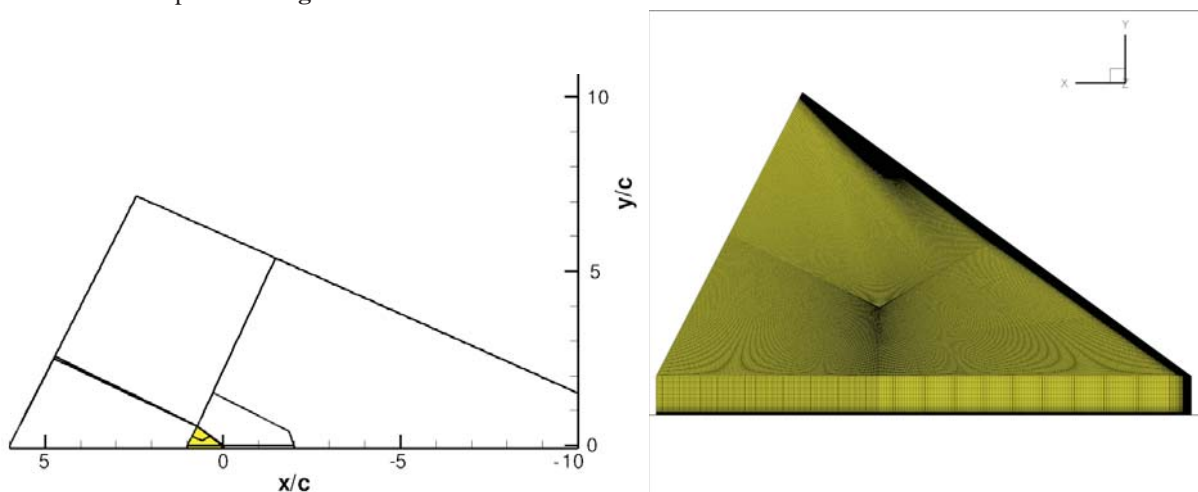


**Figure A-2. Computational domain and grid details.**

In addition, the peniche as well as the floor boundary layer have been taken into account. A wall slip condition is applied for  $-10 < x/c_r < -2$  and an adiabatic non-slip condition is applied for  $x/c_r > -2$ .

The common test conditions for NACA 64A006 wing have been retained:

- $\alpha = 12$  deg.
- $M = 0.15$
- $R_{mac}$  (based on m.a.c. = 0.8m) =  $2.74 \times 10^6$  (accordingly, total pressure: 1bar, total temperature: 288 K)

The present study has been realized thanks to the FLU3M code developed at ONERA. This code solves the compressible Navier-Stokes equations on multiblock structured grids. The time integration is carried out by means of the second order accurate backward scheme of Gear. The simulations are performed on 32 quadri-core processors Nehalem X5560. The CPU cost per cell and per inner iteration is about  $3 \times 10^{-6}$ s.

The time-step of the calculation is fixed to  $\Delta t_{CFD} = 10^{-6}$ s, which corresponds to a non-dimensional time step  $\Delta \tilde{t} = \Delta t_{CFD} (U_0 / c) = 4.25 \times 10^{-5}$ . Temporal accuracy of the calculation was checked during the inner iteration

process (four Newton-type inner-iterations are used to reach second order time accuracy). A decrease of the inner-residuals of at least one order is obtained.

### C. Results and Discussion

#### 1. Reynolds averaged data and Aerodynamic Loads.

The pressure coefficient on the wing is displayed in **Figure A-3** for both RANS (SA<sup>27</sup> & SARC<sup>30</sup>) and ZDES calculations. Free stream is from the right, and the flow is mainly organized around a main vortex sheet named  $V_I$  in the figure. Of interest, the footprint of a second vortex  $V_{II}$  is only obtained with the ZDES calculation.

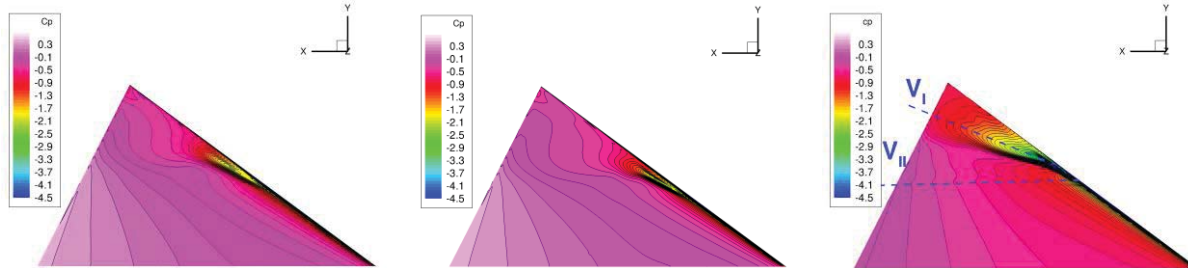


**Figure A-3.** Mean pressure distribution  $C_p$  on the wing. From left to right: RANS-SA / RANS-SARC / ZDES.

Concerning the RANS calculations, it is worth noting that the separation occurs earlier when the rotation correction is active. The most downstream location of separation onset is provided by the ZDES calculation where a much more spread out aspect of the  $C_p$  distribution characterizing flow unsteadiness is observed.

To get a more quantitative insight, **Figure A-4** displays the  $C_p$  distribution in different sections along the wing. While no differences are observed between the different calculations for  $x/c_r \leq 0.305$ , both RANS calculations indicate a nearly constant pressure level at the most downstream location (e.g.,  $x/c_r = 0.6$ ).

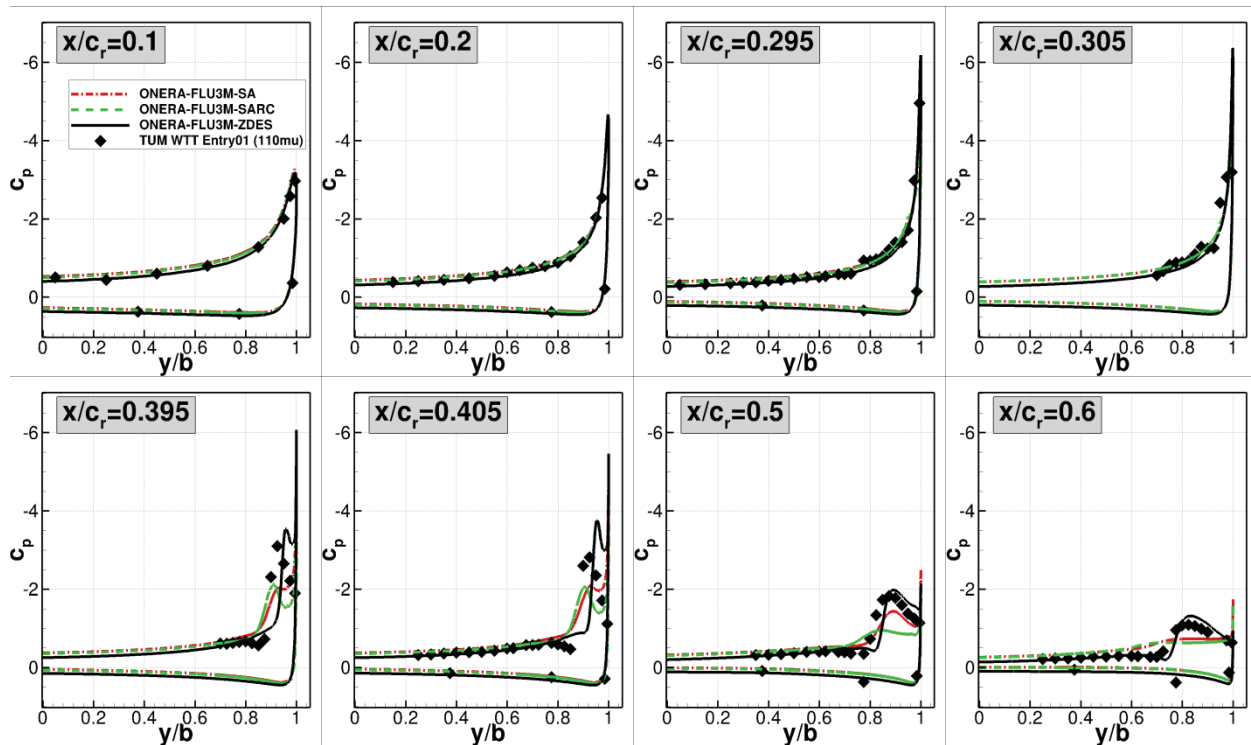


**Figure A-4.** Mean pressure distribution  $C_p$  at several sections along the wing. ( $b$  is the local wing semispan).

Though the pressure distribution on the wing is then dramatically modified, only minor differences are observed on the force coefficients as shown in **Table A-1**. Indeed, the values of the lift coefficient are nearly the same and an approximately 8% lower value of the drag coefficient is observed for the ZDES calculation.

**Table A-1. Force coefficients with the wing alone.**

Numerical Model	$C_D$	$C_L$
RANS-SA	0.0942	0.607
RANS-SARC	0.0969	0.597
ZDES	0.0877	0.609

To get further physical insight into this flow, the unsteady properties of the aerodynamic field are investigated in the next section.

## 2. Pressure and Velocity Fluctuation

To begin with, **Figure A-5** highlights the distribution of pressure fluctuations,  $C_{p,rms} = P_{rms}/(\frac{1}{2}\gamma M_0^2 P_0)$ , on the upper side of the wing. Free stream is again from the right, and let us be reminded that in the framework of mode 2 of ZDES, the attached boundary layers are treated in URANS mode so that the separated flow is responsible for the unsteady character of the wall pressure field. Note that the footprint of the unsteady flow over the wing is highly three-dimensional and though qualitative, the extent of the “dynamically active area” is of interest to focus the area of experimental investigation. The onset of separation occurring near the middle of the leading edge is clearly visible. The highest levels of pressure fluctuations, which can reach up to 40% of the free-stream dynamic pressure, are located in the impingement region of the main vortex sheet  $V_1$ .

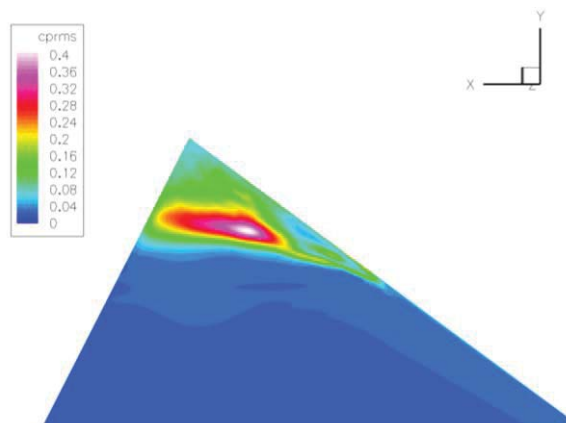


**Figure A-5.  $C_{p,rms}$  distribution on the wing.**

The Power Spectral Density (PSD) function of pressure fluctuations, named  $G(f)$  and expressed in  $\text{Pa}^2/\text{Hz}$  describes how the mean squared-value of the wall pressure previously described is distributed in frequency since:

$$P_{rms}^2 = \int_0^\infty G(f) df \quad (\text{A-3})$$

Several sensors along four lines named  $L_1$  to  $L_4$  have been defined and are plotted in **Figure A-6** together with a snapshot of the wall pressure distribution. As an example, the spectral map ( $f c/U_0$ ,  $x/c$ ) of pressure fluctuation for line  $L_2$  located under the main vortex sheet is given in Figure A-6. Note that the frequency range is given both in Hertz (relevant for the design of the experiment) and normalized by the free-stream velocity  $U_0$  and the root chord  $c$  (i.e.,  $St_c = f c/U_0$ ) in order to better identify physical phenomena.

Two slices named respectively a) and b) at stations  $x/c_r = 0.62$  and  $0.68$  are extracted from this spectral map. The bandwidth of the pressure signal is observed for normalized frequencies  $f c/U_0 \leq 35$ . In addition, the spectrum at  $x/c_r = 0.62$  displays sharp peaks that emerge from the broadband content. The main peak is observed at  $St_c \approx 14$  together with its first sub-harmonic at  $St_c \approx 7$ . Further downstream at station  $x/c = 0.68$ , the relative intensity of the fundamental frequency decreases to the benefit of its sub-harmonics. This behavior is characteristic of the merging process of the large-scale structures populating the mixing layer in the main vortex sheet. Note that the corresponding physical length scale  $\lambda$  is given by:

$$\frac{\lambda}{c} = \frac{U_0}{f c} = \frac{1}{St_c} \approx \frac{1}{14} \approx 0.071 \quad (\text{A-4})$$

which corroborates with the length  $\lambda \approx 0.066 c$  identified on the instantaneous footprint of the wall pressure.

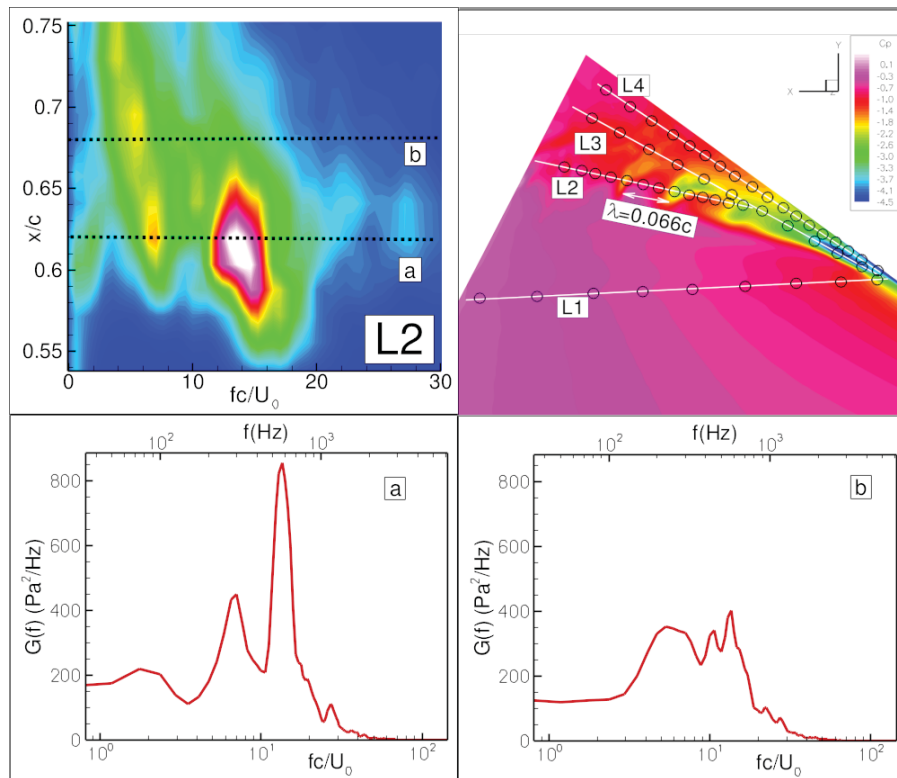


**Figure A-6. PSD of wall pressure fluctuations. Top left: spectral map along line L2; Top right: instantaneous wall pressure. Bottom: PSD at  $x/c_r = 0.62$  (rake a) and  $x/c_r = 0.68$  (rake b).**

It is worth adding that numericists have at their disposal the temporal evolution of all hydrodynamic quantities in the entire volume of the flow with the best accuracy, which allows a deep investigation of the flow physics. As an example, **Figure A-7** shows the turbulent structures evidenced by showing a positive value of the  $Q$  criterion. Let us be reminded that it defines as vortex tubes the regions where the second invariant of velocity gradient tensor  $Q = \frac{1}{2}(\|\Omega\|^2 - \|S\|^2)$  is positive where  $S$  and  $\Omega$  denoting, respectively, the strain and the rotation tensor.

The roll-up of two main vortex sheets named  $V_I$  and  $V_{II}$  can be clearly identified together with the wake evidenced by the total pressure loss. In addition, one may notice a cross flow instability near the root of the wing, the study of which is beyond the scope of this paper.

Besides, several sensors have been defined inside the flow field as highlighted in **Figure A-8**. One can notice that spectra of streamwise velocity display a very broadband aspect since energy is observed up to frequencies  $St_c \approx 200$ . The spectra of sensor V60 and V61 clearly highlight the vortex merging dynamics (Kelvin-Helmholtz instability) at  $St_c \approx 7-14$  in the mixing layer surrounding the vortex

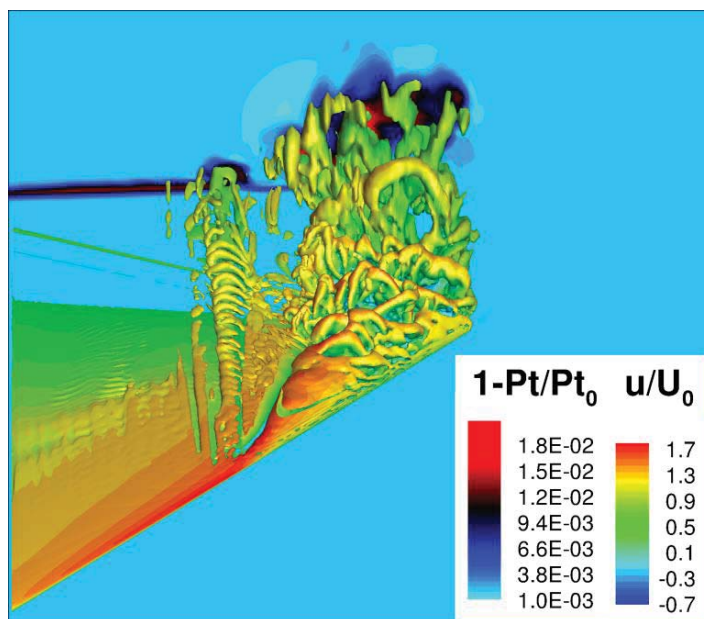


**Figure A-7. Turbulent structures educed by the  $Q$  criterion colored by the streamwise velocity with the total pressure loss in background.**

sheet  $V_I$ . As an example, the spectrum for sensor V61 displays a peak near  $f \approx 600 \text{ Hz}$  (or  $St_c \approx 14$ ). This frequency can be compared with that given linear stability theory<sup>31</sup>, which indicates that the two-dimensional linearly most unstable mode has a streamwise wave number nearly equal to  $7 \delta_\omega$  where  $\delta_\omega$  is the vorticity thickness defined by:

$$\delta_\omega = \frac{\Delta U}{\max_N \left( \frac{dU}{dN} \right)} \quad (\text{A-5})$$

where  $\Delta U = (U_{high} - U_{low})$  denotes the difference between the local maximum and minimum velocities and  $N$  the shear-normal direction. The most amplified frequency for a spatially developing mixing layer between two streams with respective velocity  $U_{high}$  and  $U_{low}$  may be given by:

$$f_\omega = ((U_{high} + U_{low}) / 7\delta_\omega) / 2 \quad (\text{A-6})$$

One can then compute the local vorticity thickness  $\delta_\omega$  from the local wall-normal velocity profile crossing sensor V61 and one gets  $\delta_\omega/c \approx 6 \times 10^{-3}$  leading to  $St_\omega = f_\omega c / U_0 \approx 12$ , which is not so far from the observed frequency content in Figure A-8 since the present mixing layer differs from a planar one.

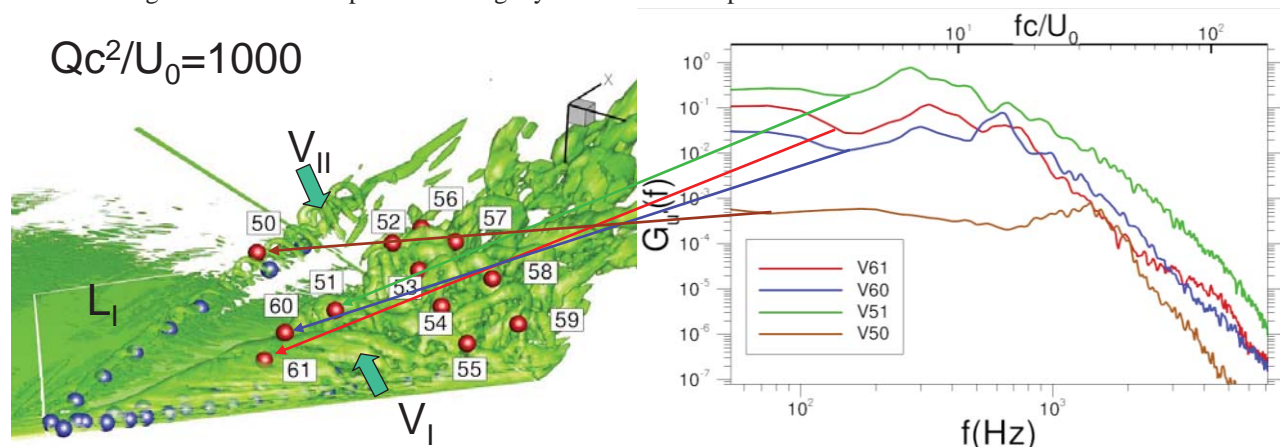


**Figure A-8. Left: iso surface of the Q criterion and location of sensors (the blue symbols indicate wall pressure sensors and the red symbols indicate sensors located in the flow field). Right: PSD of the streamwise velocity component  $u'$  at discrete locations.**

Sensor V50 is located in the second vortex  $V_{II}$  whose separation onset occurs close to the leading edge of the wing. This vortex grows close to the wall and the fine scale structures feature a much higher frequency dynamics since a spectral hump is observed near  $St_c \approx 30$ . Let us mention that this latter is not simulated neither with the present SA nor SARC calculations (see Figure A-3). Nevertheless, the energy content of vortex  $V_{II}$  is small compared with the one of  $V_I$ .

This dynamics characterized by spectral humps emerging from the broad banded spectral content affects the whole aerodynamic field as can be depicted from showing the PSD of the lift and drag coefficients, **Figure A-9**. The knowledge of the spectral content of the dynamic loads may be of interest in the framework of both aero-structural and aerodynamics/flight mechanics coupling.

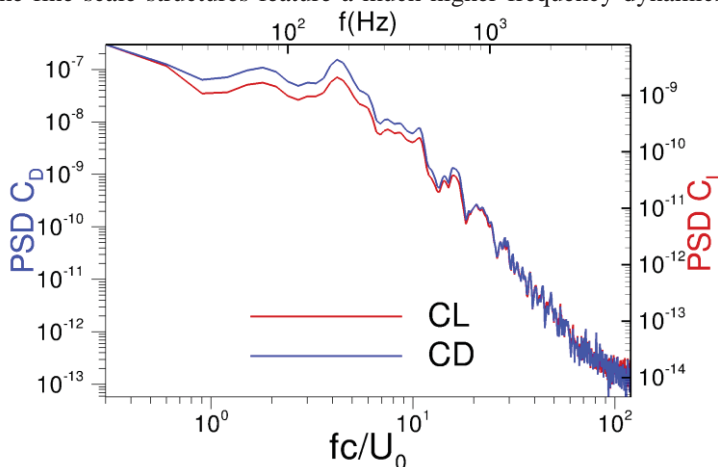


**Figure A-9. PSD of Lift and Drag components.**

## IX. References

- <sup>1</sup>Cummings, R.M., Schütte, A., “Integrated Computational/Experimental Approach to Unmanned Combat Air Vehicle Stability and Control Estimation”, *AIAA Journal of Aircraft*, Vol. 49, No. 6, pp. 1542-1557, Nov-Dec 2012. (See also AIAA 2010-4392, Jun 2010).
- <sup>2</sup>RTO. “Assessment of Stability and Control Prediction Methods for NATO Air & Sea Vehicles,” RTO-TR-AVT-161, Sep. 2012.
- <sup>3</sup>Schütte, A., Hummel, D., and Hitzel, S., “Flow Physics Analysis of a Generic Unmanned Combat Aerial Vehicle Configuration”, *AIAA Journal of Aircraft*, Vol. 49, No. 6, pp. 1638-1651, Nov-Dec 2012. (See also AIAA 2010-4690, Jun 2010).
- <sup>4</sup>Luckring, J.M., and Boelens, O.J., “A Reduced-Complexity Investigation of Blunt-Leading-Edge Separation Motivated by UCAV Aerodynamics,” AIAA 2015-xxxx, Jan. 2015.
- <sup>5</sup>Hövelmann, A., Knoth, F., and Breitsamter, C., “Leading-Edge Roughness Effects on the Flow Separation Onset of the AVT-183 Diamond Wing Configuration,” AIAA 2015-xxxx, Jan. 2015.
- <sup>6</sup>Hövelmann, A., Grawunder, M., Buzica, A., and Breitsamter, C., “Experimental Analyses on the Flow Field Characteristics of the AVT-183 Diamond Wing Configuration,” AIAA 2015-xxxx, Jan. 2015.
- <sup>7</sup>Visonneau, M., Toxopeus, S., and Guilmineau, E., “Incompressible flow calculations of blunt leading edge separation for a 53 degree swept diamond wing,” AIAA 2015-xxxx, Jan. 2015.
- <sup>8</sup>Daniel, D.T., Malloy, D.J., Morris, C.C., Gaudenkauf, J., and Reasor D.A., Jr., “Numerical Investigations of Flow Separation on the AVT-183 53 Degree Swept Diamond Wing Configuration,” AIAA 2015-xxxx, Jan. 2015.
- <sup>9</sup>Reasor D.A., Jr., Malloy, D.J., and Daniel, D.T., “Applicability of Hybrid RANS/LES Models in Predicting Flow Separation Onset of the AVT-183 Diamond Wing,” AIAA 2015-xxxx, Jan. 2015.
- <sup>10</sup>Frink, N.T., “Numerical Analysis of Incipient Separation on 53° Swept Diamond Wing,” AIAA 2015-xxxx, Jan. 2015.
- <sup>11</sup>Hitzel, S.M., Hövelmann, A., and Boelens, O.J., “Vortex Development on the AVT-183 Diamond Wing Configuration – Numerical and Experimental Findings,” AIAA 2015-xxxx, Jan. 2015.
- <sup>12</sup>Edefur, H., Tormalm, M., and Nangia, R., “Numerical study of blunt leading edge separation on a 53 degree swept diamond wing (STO AVT-183) using the Edge and Cobalt flow solvers,” AIAA 2015-xxxx, Jan. 2015.
- <sup>13</sup>Tomac, M., and Rizzi, A., “CFD Study of Vortex Separation Phenomena on Blunt Diamond Wing,” AIAA 2015-xxxx, Jan. 2015.
- <sup>14</sup>Ghoreyshi, Ryszka, Cummings, and Lofthouse, “Vortical Flow Prediction of the AVT-183 Diamond Wing,” AIAA 2015-xxxx, Jan. 2015.
- <sup>15</sup>Luckring, J.M., and Boelens, O.J., “A Unit-Problem Investigation of Blunt Leading-Edge Separation Motivated by AVT-161 SACCON Research,” RTO MP-AVT-189, Paper 27, Dec. 2011.
- <sup>16</sup>Frink, N.T., “Strategy for Dynamic CFD Simulations on SACCON Configuration,” AIAA 2010-4559, Jun 2010.
- <sup>17</sup>Frink, N.T., “Upwind Scheme for Solving the Euler Equations on Unstructured Tetrahedral Meshes,” *AIAA Journal*, Vol. 30, No. 1, 1992.
- <sup>18</sup>Hensch, M.J., and Luckring, J.M., “Connection Between Leading-Edge Sweep, Vortex Lift, and Vortex Strength for Delta Wings,” *AIAA Journal of Aircraft*, Vol. 27, No. 5, May 1990.
- <sup>19</sup>Polhamus, E.C., “A Survey of Reynolds Number and Wing Geometry Effects on Lift Characteristics in the Low Speed Stall Region,” NASA CR-4745, Jun 1996.
- <sup>20</sup>RTO. Understanding and Modeling Vortical Flows to Improve the Technology readiness Level for Military Aircraft. RTO-TR-AVT-113, Oct. 2009.
- <sup>21</sup>Boerstoel, J.W., Kassies, A., Kok, J.C., and Spekreijse, S.P., “ENFLOW, a Full-Functionality System of CFD Codes for Industrial Euler/Navier-Stokes Flow Computations,” NLR TP 96286U, NLR, Amsterdam, 1996.
- <sup>22</sup>Deck, S., “Zonal Detached Eddy Simulation of the flow around a high-lift configuration,” *AIAA Journal*, Vol. 43, pp. 2372-2384, 2012.
- <sup>23</sup>Deck, S., “Recent Improvements in the Zonal Detached Eddy Simulation (ZDES) Formulation,” *Theoretical and Computational Fluid Dynamics*, vol. 26 (6), pp. 523-550, doi:10.1007/s00162-011-0240-z, 2012.
- <sup>24</sup>Deck, S., Gand, F., Brunet, V., and Ben Khelil, S., “High-fidelity simulations of unsteady civil aircraft aerodynamics: stakes and perspectives. Application of Zonal Detached Eddy Simulation,” *Philosophical Transactions of the Royal Society A*, 372:20130325. doi:10.1098/rsta.2013.0325, 2014.
- <sup>25</sup>Tramel, R.W., Nichols, R.H., and Buning, P.G., “Addition of Improved Shock-Capturing Schemes to OVERFLOW 2.1,” AIAA 2009-3988, Jun 2009.
- <sup>26</sup>Sagaut, P. and Deck, S., “Large eddy simulation for aerodynamics: status and perspectives,” *Philosophical Transactions of the Royal Society A*, vol 367, pp 2849-2860, 2009.
- <sup>27</sup>Spalart, P.R., and Allmaras, S.R., “A one equation turbulence model for aerodynamic flows,” *Rech. Aérop.* 1, pp 5-21, 1994.
- <sup>28</sup>Deck S., Laraufige R., “Numerical investigation of the flow dynamics past a three-element aerofoil,” *Journal of Fluid Mechanics*, Vol. 732, pp. 401-444, doi:10.1017/jfm.2013.363, 2013.
- <sup>29</sup>Spalart, P. R., Deck, S., Shur, M. L., Squires, K. D., Strelets, M., and Travin, A, “A new version of detached-eddy simulation resistant to ambiguous grid densities,” *Theoretical and Computational Fluid Dynamics*, Vol. 20, pp. 181-195, 2006
- <sup>30</sup>Dacles-Mariani, J., Zilliac, G.G., Chow, J.S., Bradshaw, P, “Numerical/Experiment study of a wingtip vortex in a near-field,” *AIAA Journal*, Vol 33, No 9, 1995.

<sup>31</sup>Huerre, P., and Monkewitz, P.A., "Local and global instabilities in spatially developing flows," *Annual Review of Fluid Mechanics*, 22, pp 473-537, 1990.